

## Flow of viscoelastic surfactants through porous media

De, S.; Koesen, S. P.; Maitri, R. V.; Golombok, M.; Padding, J. T.; van Santvoort, J. F.M.

**DOI**

[10.1002/aic.15960](https://doi.org/10.1002/aic.15960)

**Publication date**

2018

**Document Version**

Accepted author manuscript

**Published in**

AIChE Journal

**Citation (APA)**

De, S., Koesen, S. P., Maitri, R. V., Golombok, M., Padding, J. T., & van Santvoort, J. F. M. (2018). Flow of viscoelastic surfactants through porous media. *AIChE Journal*, *64*(2), 773-781. <https://doi.org/10.1002/aic.15960>

**Important note**

To cite this publication, please use the final published version (if applicable). Please check the document version above.

**Copyright**

Other than for strictly personal use, it is not permitted to download, forward or distribute the text or part of it, without the consent of the author(s) and/or copyright holder(s), unless the work is under an open content license such as Creative Commons.

**Takedown policy**

Please contact us and provide details if you believe this document breaches copyrights. We will remove access to the work immediately and investigate your claim.

## **Flow of viscoelastic surfactants through porous media**

S. De<sup>1</sup>, M. Golombok<sup>2,3</sup>, S.P. Koesen<sup>1</sup>, R.V. Maitri<sup>1</sup>, and J.T.Padding<sup>4</sup>, J.F.M. van Santvoort<sup>2</sup>

1. Faculty of Chemistry and Chemical Engineering, Technische Universiteit Eindhoven, 5600 MB Eindhoven, The Netherlands
2. Faculty of Mechanical Engineering, Technische Universiteit Eindhoven, 5600 MB Eindhoven, The Netherlands
3. Shell Global Solutions Intl B.V., Grasweg 31, 1031 HW Amsterdam, The Netherlands
4. Faculty of Mechanical Engineering, Process & Energy department, Technische Universiteit Delft, 2628CB Delft, The Netherlands

## **ABSTRACT**

We compare the flow behavior of viscoelastic surfactant (VES) solutions and Newtonian fluids through two different model porous media having similar permeability: (a) a 3D random packed bed and (b) a microchannel with a periodically spaced pillars. The former provides much larger flow resistance at the same apparent shear rate compared to the latter. The flow profile in the 3D packed bed cannot be observed since it is a closed system. However, visualization of the flow profile in the microchannel shows strong spatial and temporal flow instabilities in VES fluids appear above a critical shear rate. The onset of such elastic instabilities correlates to the flow rate where increased flow resistance is observed. The elastic instabilities are attributed to the formation of transient shear induced structures. The experiments provide a detailed insight into the complex interplay between the pore scale geometry and rheology of VES in the creeping flow regime.

## 1. INTRODUCTION

The flow of viscoelastic wormlike micelle solutions through porous media is a field of extensive research due to its wide range of practical applications such as, enhanced oil recovery, drag reducing agent, paints, detergents, emulsifiers, agrochemical, inkjet printing and many others<sup>1-3</sup>. The flow of Newtonian fluids through porous media is well understood from the frame work of Darcy's law<sup>4</sup>. However, due to the complex rheology of viscoelastic surfactants the flow of viscoelastic surfactant solutions through porous geometries is not well understood<sup>5,6</sup>.

Surfactants are amphiphilic molecules consisting of a short hydrophobic tail (10-20 carbon atom) and a bulky hydrophilic head which are either neutrally, positive or negatively charged. Beyond a critical micelle concentration (CMC), the surfactant molecules spontaneously self-assemble into large aggregates known as micelles to decrease the contact of their hydrophobic tails from water<sup>7</sup>. The aggregates can have different structures like cylindrical, spherical, vesicles or lipid layers<sup>7</sup>. The structure of these micelles depends on several factors like, salinity, temperature, pH, concentration and flow parameters<sup>8</sup>. Addition of inorganic salts like sodium chloride (NaCl), sodium nitrate (NaNO<sub>3</sub>) or organic salts like sodium salicylate (NaSal) have been found to screen the electrostatic repulsion of the hydrophilic head groups, thus reducing the CMC and inducing a structural change from spherical to wormlike aggregates<sup>9</sup>. These wormlike micelles show close similarities with polymer solutions and can be even viscoelastic, but the physical properties (diameter, persistence length) can be quite different<sup>10</sup>. Worm-like micellar viscoelastic surfactant solutions are often referred to as 'living polymers'<sup>11</sup>. However, in contrast to polymers, worm-like micelles do not have a rigid covalently bonded backbone<sup>12</sup>. They are held together by relatively weak physical forces which continuously break and reform with time<sup>13</sup>.

The rheological behavior of aqueous solutions of wormlike micelles highly depends on the solution concentration<sup>16,17</sup>. Far below the overlap concentration the micellar solutions behaves

as the Newtonian solvent. On the other hand, far above the overlap concentration, Cates' model<sup>14</sup> predicts that stress relaxation can occur by reptation and formation of new end caps if the micelles break and reform faster than their reptation time scale. The linear viscoelastic response of such concentrated wormlike micellar solutions can be described by the Maxwell model that characterizes fluid viscosity and elasticity with a single relaxation time (unlike polymers having multiple relaxation times)<sup>15</sup>. In between these extremes, close to the overlap concentration, a sharp shear thickening behavior is found beyond a critical shear rate. After reaching a maximum viscosity, shear thinning behavior is observed at higher shear rates. This is believed to be due to the ability of wormlike micellar solutions to alter the structure of their macromolecular network under flow conditions, also known as shear induced structures (SIS). The characteristics of SIS and its origin has been extensively explored in the literature by a combination of different rheological techniques and small angle neutron scattering (SANS). The complex rheological behavior is attributed to a change in the balance between the formation and destruction of the shear induced structures<sup>17-20</sup>. Once SIS form during the shear-thickening stage, the fluid also appears to become highly viscoelastic. Experimentally this has been shown by comparing results of oscillatory measurements between pre-sheared and non-pre-sheared fluids<sup>21</sup>. The fluid that was pre-sheared within the SIS regime showed significant strong elastic behavior. By contrast, tests performed without pre-shear yielded no viscoelastic response. This indicates a transition from a viscous to a viscoelastic fluid induced by the formation of SIS. Hu et al.<sup>22</sup> performed a set of rheological and flow birefringence studies on the aqueous Cetyl trimethyl ammonium bromide - sodium salicylate (CTAB/NaSal) solution in the concentration range of 0.5-5 mM. They found the shear thickening regime is highly flow birefringent, strongly nonlinear viscoelastic and possesses long relaxation times. In the dilute concentration range, the CTAB/NaSal solution is also found to exhibit a much higher extensional viscosity compared to the shear viscosity<sup>23</sup>.

Despite the extensive applications of viscoelastic surfactants, experimental and numerical investigations of complex fluid flows through porous media are mostly limited to inelastic non-Newtonian fluids or to viscoelastic polymers<sup>5</sup>. Experimentally, the onset of elastic instability and increased pressure drop was reported for the flow of viscoelastic polymers through straight, curved channels and model porous media in the creeping flow regime<sup>24–30</sup>. Numerical investigation of viscoelastic fluid flow has been performed using finite volume, finite element and particle based simulations<sup>31–36</sup>, employing Oldroyd-B, Giesekus, FENE and other viscoelastic models. Simulations of viscoelastic fluid flows are mostly performed through an array of spheres or cylinders periodically placed to constitute a model porous medium<sup>34,37,38</sup>. Most researchers have tried to link the increased flow resistance found in viscoelastic fluid flows through porous media to enhanced extensional effects<sup>39,40</sup>. However, our recent work on viscoelastic fluid flow through symmetric and asymmetric periodic sets of cylinders shows that most viscoelastic energy dissipation occurs in the shear-dominated regions of the flow domain, not in extensional-flow-dominated regions<sup>41</sup>.

The flow of wormlike micelles through model porous medium was also studied recently<sup>17,42–46</sup>. Rojas et al.<sup>42</sup> investigated the flow of wormlike micellar solutions formed by oppositely charged mixtures of cationic cetyl trimethylammonium *p* – toluene sulfonate (CTAT) and anionic sodium dodecyl sulfate (SDS). They found an increased shear thickening in porous media flow. The increased flow resistance was attributed to the synergistic effect of shear and extension in the porous configuration<sup>17</sup>. Vasudevan et al.<sup>43</sup> showed the existence of irreversible nanogel formation for flow of VES solution comprised of CTAB/NaSal through a porous media packed with glass beads. They showed that at extremely high deformation rate ( $> 10^4 \text{ s}^{-1}$ ), stable gel-like structures are formed, which they termed as Flow Induced Structured Phase (FISP). A similar FISP formation was also reported by Cardiel et al.<sup>46</sup>. Flow of wormlike micellar solutions through a periodic array of cylinders was performed by Moss et al.<sup>5</sup>. They observed

presence of spatio-temporal flow instabilities; however, the formation of SIS was not reported. A combined experimental and numerical work on entangled wormlike micellar fluids was performed by Boek et al.<sup>15</sup>. Very recently Zhao et al.<sup>44</sup> reported the flow instability of wormlike micellar solutions past a single cylinder over a range of shear rates. However, a detailed study correlating such elastic instabilities with increased flow resistance for flow of viscoelastic surfactants in porous media is still not established.

In case of oil field applications the flow of viscoelastic surfactants are mostly performed in core samples extracted from the field. Such experiments only provide a correlation between the applied flow rate and pressure drop. In these experiments, detailed inspection of the flow structures at the pore level is very difficult. However, microfluidic devices can mimic a model porous medium, as length and time scales that are similar to applications pertaining to porous media flow<sup>47</sup>. As discussed, a complete understanding between the complex interplay between the rheology of viscoelastic surfactant and pore structure is still missing. Moreover, a comparative study of flow behavior of viscoelastic surfactants in a packed bed and a pillared microchannel (representing a model porous media) has never been reported in the literature.

Motivated by this, in this work we study the behavior of both Newtonian fluids and viscoelastic surfactant solutions through two different porous media of similar permeability, namely a three dimensional packed bed consisting of monodispersed spheres and a pillared microchannel representing a model porous medium. In both cases, an increased flow resistance after a critical apparent shear rate was observed, compared to Couette flow measurements. The cause of the enhanced pressure drop and its relation to elastic instabilities for viscoelastic surfactants, was further investigated by the flow measurements using the pillared microchannel.

The paper is divided in three sections. First we describe both the experimental set up and the materials used. Second we explain the results from the core flow and microfluidic experiments. Finally we compare the results from the different experiments and characterize the elastic

effects through flow visualization.

## 2. EXPERIMENT

### 2.1 Materials

Cetyl tri-methyl ammonium bromide (CTAB) and sodium salicylate (NaSal) (Sigma Aldrich) at a purity of > 99% and > 99.5% is used to prepare the viscoelastic surfactant solution. In this work we indicate a VES fluid as a “ $x/y$ ” solution containing  $x$  mM CTAB and  $y$  mM NaSal. The base fluid for the VES solution is a synthetic brine of demineralized water with 3wt% NaCl. After the solutions are prepared they are kept at room temperature (22<sup>0</sup>C), while magnetically stirring them for 12 hours to ensure that all components are fully dissolved.

### 2.2 Rheological characterization

The rheological characterization of the VES fluids, is performed using an Anton Paar MCR302 rheometer at 22<sup>0</sup>C. This device uses a double-gap geometry to measure the shear response. The tests are performed for a shear rate range of 1 – 1000 s<sup>-1</sup> which covers the shear rates typically found in porous media flows. The shear response of the three different equimolar CTAB/NaSal solutions in 3wt% NaCl demineralized water is shown in figure 1. The rheological measurements are repeated thrice to ensure reproducibility. All VES solutions show the characteristic non-monotonic shear-thickening/shear-thinning behavior consistent with other literature results<sup>23</sup>. The VES solution with the lowest concentration (1.0/1.0 mM) has the lowest zero shear viscosity ( $\mu_0 = 1.2$  mPa · s) and a maximum viscosity (when the shear thickening plateau is reached),  $\mu_{max} = 1.9$  mPa · s. The critical shear rate ( $\gamma_c$ ), defined as the shear rate where the onset of shear thickening occurs is found to be 365 s<sup>-1</sup>. A list of critical shear rates and viscosities determined from the shear rheometer for different CTAB/NaSal concentration is listed in table 1. The rheology data shows that both  $\mu_0$  and  $\mu_{max}$  increase with CTAB/NaSal concentration. This suggests that there is a stronger micellar network present at higher concentrations. Also the critical shear rate ( $\gamma_c$ ) decreases with increased concentration.

The critical shear rate for the onset of shear thickening gives a measure of the onset of SIS formation, and entanglements of the wormlike micelles. Thus the inverse of this critical shear rate ( $\tau_c = 1/\dot{\gamma}_c$ ) provides an idea of typical relaxation time of such entanglements<sup>42</sup>. Figure 2 shows how the typical relaxation time ( $\tau_c$ ) increases with increase in CTAB/NaSal molar ratio.

### **2.3 Macrofluidic setup (core flow experiment)**

The core flow setup designed to test the response of the VES fluids in porous media is shown in figure 3. The main component of the experiment is a core-holder in which the sintered glass core is placed. The core holder is filled with compressed air at 6 bar to force a tight seal between the rubber sleeve and the core. This ensures axial flow. The core holder is positioned vertically to force air out at the top when saturating the cores. Fluid flow is controlled using a Quizix pump (QX 6000 HC pump) with a flow rate range of 0.001 – 50 ml/min. The associated pressure drop driving the flow is measured using a pressure transducer (Rosemount 3051CD 5) with an operating range of -20.5 to +20.5 bar. The entire setup is housed in a temperature controlled chamber set to 22 °C.

Prior to each experiment the core is placed in an oven at 250 °C to evaporate all remaining fluids from previous experiments. When the core is positioned inside the core-holder, CO<sub>2</sub> is flushed through to displace the air inside the pores of the core. Next the pump saturates the core with brine and the absolute brine permeability of the core is determined by measuring the pressure drop for 5 different flow rates and applying Darcy's law. The permeability of the core is found to be approximately 4400 mD.

Next the core is saturated with VES and all the brine is displaced from the core. To determine the response of the VES fluid, the flow rate is gradually increased between 1 and 15 ml/min. At low flow rate a steady pressure is obtained. However, at higher flow rates sufficient time is given (minimum 40 minutes) to stabilize the flow after which the pressure drop is obtained from the pressure transducer. The pressure drop data ( $\Delta P$ ) and the set flow rate ( $q$ ) in

combination with the known permeability ( $\kappa$ ) and flow area (A) can be used to find the macroscopic Darcy viscosity of the fluid using Darcy's law:

$$\mu_{\text{app}} = \frac{\kappa \cdot A \Delta P}{q L} \quad (1)$$

The use of this equation to find the viscoelastic response of the fluid is further explained in the next section. After each experiment demineralized water is injected to displace the VES fluid and the core is placed in an oven to dry-out. The flow experiments are repeated thrice to ensure reproducibility.

## 2.4 Microfluidic setup

The microfluidic experiments are performed using a rectangular microchannel etched in a silicon wafer of length 6.6 cm, a width of 1 mm and a height of 50  $\mu\text{m}$ . Inside the channel there is an array of cylindrical pillars in a stretched hexagonal pattern as shown in figure 4. The distance along the flow direction (x) of two successive pillars ( $X_p$ ) and along the width (y) of the channel ( $Y_p$ ) is shown in table 2 for different channels. All pillars are modified with a hydrophilic coating. A detailed description of the manufacturing of microchannel and properties has been reported elsewhere<sup>48</sup>.

We slowly change the flow rate of the injected solutions using a KR Analytical syringe pump of capacity 5000  $\mu\text{l}$  and flow rate 0.02 - 30000  $\mu\text{l}/\text{min}$ . The pillared microchannel is placed on a Zeiss Axio Observer D1, which is an inverted microscope. For the flow visualization, the fluid is seeded with 1  $\mu\text{m}$  fluorescent tracer particles (Nile Red, Molecular probes, Invitrogen, Density: 1055  $\text{kg}/\text{m}^3$ , Excitation range 535 – 575 nm, 0.02 wt %). Images are captured using a Redlake Motion Pro X-4 camera mounted on the top of the microscope. The experimental setup is similar to the previously described set up of Sousa et al.<sup>49</sup>. The depth of field of the microscope was calculated to be 10% of the height of the microchannel. The flow path lines are visualized in a focal plane in the center between the top and bottom walls so any effect of out

of plane velocity gradients can be minimized. Bright field images are captured using a high intensity directed light source to excite the tracer particles. A green filter (500 – 600 nm) is used to filter any other light except the light from the particles.

A Sensor Technics (Puchheim, Germany) micro pressure sensor is connected to the channel to measure the pressure drop. The range is 0-2 bar, with a temporal resolution of 1 ms. At low flow rates it was possible to reach a steady pressure, but at higher flow rates the pressure signal had more fluctuations. The images were processed using Davis and Matlab software packages. Images are obtained with a resolution of 512 x 512 pixels.

The flow is studied in a square section (around 66% of the channel width) close to the middle section, lengthwise. The images are captured at a frame rate of 60 fps, which is much faster than the time scale of fluid flow. In between experiments the channel is cleaned by water injection at 300  $\mu\text{l}/\text{min}$  followed by air flushing. All flow experiments are repeated to ensure reproducibility.

### **3. RESULTS**

Both porous media, namely the packed bed and the P5 microfluidic channel, have similar permeability based on Darcy flow measurements. We first analyze the flow behavior of VES through the core and pillared microchannel individually and then compare the different flow responses for different VES concentrations. Next we observe the complex flow behavior of VES on the basis of flow instabilities as analyzed from microchannel experiments. For all our experiments, we have kept the Reynolds number  $\text{Re} = \rho U \sqrt{k} / \eta$  less than 0.01, so any inertial effects can be neglected. Here  $U$  is the average flow velocity (averaged across the space between the pillars),  $\rho$  is the fluid density,  $\eta$  is the fluid viscosity, and  $k$  is the permeability determined from brine experiments. The other important dimensionless number for our experiments is the Deborah number (De), which is the ratio of the relaxation time of the polymer and a characteristic time scale of the flow. This characteristic time scale is usually taken to be

the time needed for the average flow to pass a certain length scale, characteristic for the experiment. Here we use the characteristic length scale to be  $\sqrt{k}$ . Based on this, the De number is defined as  $De = \tau_c U / \sqrt{k}$ . The ratio of De and Re number is known as elasticity number  $El = \tau_c \eta / k \rho$ , which is independent of the flow kinematics and depends only on the fluid rheology and the characteristic size of the porous medium. These non-dimensional numbers are very important to characterize the flow in both core flow and microchannel.

### 3.1 Core flow results

Figure 5 shows the flow rate against pressure gradient for VES solutions flowing through the 4400 mD sintered glass core. The dashed line represent the response for brine. Brine shows a clear Newtonian response where the flow rate is linearly correlated to the pressure gradient following Darcy's law for Newtonian fluids. The VES solutions at low pressure gradient ( $\Delta P/L < 0.1$  bar/m) also show a linear response between flow rate and pressure gradient due to the presence of a pseudo-Newtonian regime. However, as the pressure gradient is increased the VES graphs depart from this linear (Newtonian) behavior. At similar pressure gradient, the 2/0/2.0 mM VES solution deviates the most from the Newtonian behavior compared to 1.5/1.5 mM and 1.0/1.0 mM solution. This behavior is analogous to the rheological response based on Couette flow measurements as shown in figure 1.

For a viscoelastic fluid, the viscosity is not a constant but generally depends on the flow conditions. However, we can still define an apparent viscosity by using Darcy's law. Dividing the apparent viscosity by its low flow rate limit gives us insight in the effective flow-induced thinning or thickening of the fluid in the porous medium. In detail, the resistance factor ( $\Lambda$ ) of a viscoelastic fluid flowing with a volumetric flow rate  $q$  and pressure drop  $\Delta P$  through a porous medium is given by:

$$\Lambda = \frac{\left(\frac{\Delta P}{q}\right)_{VES}}{\left(\frac{\Delta P}{q}\right)_N} \quad (2)$$

The subscript *VES* indicates viscoelastic surfactant at a specific flow rate or pressure drop, while the subscript *N* indicates its Newtonian low flow rate or low pressure drop limit. The resistance factor  $\Lambda$  is similar to the definition of dimensionless apparent viscosity or also known as apparent relative viscosity<sup>41</sup>.

Figure 6 shows the resistance factor versus flow rate for three equimolar VES fluids through a 4400 mD sintered glass core. At low flow rate the resistance for all fluids are relatively constant and close to 1. The apparent viscosity in the porous cores is similar to the viscosity of the brine base fluid (eq. 1). Increasing the flow rate results in a departure from this quasi-Newtonian behavior and an increase in the resistance factor. Similar to couette flow measurements, the resistance factor for the 2.0/2.0 solutions not only increases at a lower flow rate, but the magnitude of shear thickening<sup>41</sup> is also greater compared to the other solutions. This illustrates that the network formed for the 2.0/2.0 solution is stronger, which results in a significantly higher increase in resistance factor compared to the other equimolar solutions. The enhanced viscosity can be attributed to the viscoelastic effects, which will be discussed later from our flow characterization study.

### 3.2 Microfluidics results

Figure 7 shows the flow rate to pressure gradient response for brine and 2.0/2.0 mM VES solution in the P16 micro-channel. Initially the response of the 2.0/2.0 solution is nearly identical to brine. This indicates pseudo-Newtonian behavior at low pressure gradient. However, at increased pressure gradient, the flow behavior of the 2.0/2.0 solution starts to deviate from brine. At equal pressure gradient the flow rate of the 2.0/2.0 solution is significantly lower than that of brine as we have observed in the sintered glass core measurements. This signifies an increased flow resistance for the VES solution.

Similar to the core flow experiment, the deviation from pseudo-Newtonian behavior can be investigated by introducing the resistance factor ( $\Lambda$ ). The absolute permeability  $\kappa$  here is the permeability of the pillared micro-channel derived from brine measurements and  $L$  is the length of the micro-channel. Equation 2, is used to find the resistance factor at different flow rates in both pillared micro-channels. This is plotted against the flow rate in Figure 8 for a 2.0/2.0 mM VES solution in both the P5 and P16 micro-channel. When the flow rate is sufficiently low, ( $< 0.2 \mu\text{l}/\text{min}$ ), the resistance factor is approximately 1.0 for both the channels. This indicates that the flow behavior is pseudo-Newtonian in nature. When the flow rate is further increased the SIS starts to form and thus the resistance factor also increases. Figure 8 shows that the resistance factor increases at a lower flow rate in the P5 microchannel where the distance between the pillars is smaller compared to P16 channel. At the same flow rate, the P5 channel leads to a higher shear rate and deformation. The SIS network will thus form at a lower flow rate, transforming the fluid from a viscous to a viscoelastic fluid<sup>22</sup>. This leads to the increase in the resistance factor as shown in figure 8. Not only is the onset of viscoelasticity at a lower flow rate in the P5 channel, also the magnitude of the increased resistance is higher (The maximum flow resistance is 44 times in P5 channel compared to 17 times in P16 channel compared to Newtonian brine solution). As we shall see in the following section on microscopic effects, this is caused by the increased complexity of the flow due to additional flow perturbations caused by more pillars at smaller spacing.

The resistance factor for three different equimolar concentration of VES fluids in similar range of flow rate is shown in figure 9. Similar to our couette flow observations, the 2.0/2.0 mM solution starts to shear thicken at a much lower flow rate compared to the other two solutions. Further the maximum flow resistance is also higher, 17 times more than brine, in the 2.0/2.0 mM solution, compared to approximately 5 and 2 times more than brine in 1.5/1.5 and 1.0/1.0 mM solution, respectively. This shows that a higher concentration of equimolar CTAB/NaSal

promotes SIS formation.

The results from the micro-channel can now be compared to the results from the core flow tests. The permeability of the P5 micro-channel is comparable to the permeability of the sintered glass core. In order to make a comparison between them the flow rate is replaced by the apparent shear rate for both experiments. For porous flow through the sintered glass core the apparent shear rate can be determined via the following equation<sup>32</sup>:

$$\gamma_{app,core} = \frac{4 \cdot \alpha \cdot u}{\sqrt{8\kappa/\varepsilon}} \quad (3)$$

In this equation  $u$  is the interstitial flow velocity and  $\alpha$  is a correction factor equal to 2.5 used for packed bed geometries. The microchannel flow rate is converted to an apparent shear rate by using the brine permeability calculated during brine tests:

$$\gamma_{app,mic} = \frac{u}{\sqrt{\kappa}} \quad (4)$$

These results are plotted in figure 10, where the Couette flow results are also shown. The critical shear rate where thickening occurs overlaps for the micro-channel and the sintered glass core but not with the rheometer results. This can be attributed to the fact that the shear rate in a rheometer is constant. By contrast, the complex flow inside the pillared micro-channel and the sintered glass cores results in local microscopic variations in shear rate. The local shear rate might be substantially higher than what is calculated in eq. 3 and 4 which represents a spatial average. Locally the shear rate becomes high enough for the formation of a SIS network which increases the flow resistance.

Vasudevan et al.<sup>43</sup> showed when the deformation rate ( $S$ ) is more than  $10^6 \text{ s}^{-1}$ , stable gel like structures (FISP) are formed. Here the deformation rate ( $S$ ) is obtained from the Kozeny-Karman<sup>4</sup> relationship as

$$S = \frac{150q(1-\varepsilon)^2}{D_p^2 H \varepsilon^3} \quad (5)$$

where  $q$  is the flow rate,  $D_p$  is the particle diameter,  $H$  is the bed height, and  $\varepsilon$  is the porosity. From our core flow experiments the value of  $S$  at the highest shear rate ( $\sim 100 \text{ s}^{-1}$ ) for the 2.0/2.0 mM VES solution is approximately  $2 \times 10^8 \text{ s}^{-1}$ . The order of strain is also higher than the required strain rate needed to form gels<sup>43</sup>. However, the value of  $S$  in the pillared microchannel (P5) for a similar shear rate was around  $9.0 \times 10^5$  (and lower for P16 channel). So the 3D packed bed induces a deformation rate which is approximately twice as large as in the microchannel. Such a high deformation rate is sufficient to form stable FISP. This deformation is due to stronger confinement effects and lower porosity of the 3D bed which promotes stronger extensional and shear flow. So in spite of its similar permeability, the pillared microchannel does not provide enough deformation and strain to form stable FISP (also observed from the flow characterization study). This explains the higher flow resistance in the core flow compared to the pillared microchannel.

### 3.3 Flow characterization

A visual analysis of the trajectories of fluorescent particles is performed using the probability density function within the pillared microchannel. Figure 11 shows the occupancy graph of tracer particles which gives the flow trajectory in the P16 microchannel at different flow rates. The occupancy graph is obtained using the following formula:

$$\tilde{I}(i, j) = \frac{\sum_{n=1}^N I(n, i, j)}{\sum_{n=1}^N \sum_{p=1}^{512} \sum_{q=1}^{512} I(n, p, q)} \quad (6)$$

Where,  $I(n, i, j)$  denotes the intensity of a pixel  $(i, j)$  in the  $n^{\text{th}}$  image in an obtained time series of images. The normalized intensity at a given pixel,  $\tilde{I}(i, j)$  is obtained using eq. 6. For the current flow visualizations,  $N = 25$  images are used. Figure 11 (a) shows that a laminar flow profile is observed for the Newtonian brine solution at a relatively large flow rate of  $3 \mu\text{l}/\text{min}$  as expected for a non-inertial flow regime. The VES solution (2.0/2.0 mM) also shows a symmetric flow profile at  $0.5 \mu\text{l}/\text{min}$  ( $De = 0.4$ ) (fig. 10b). At  $2 \mu\text{l}/\text{min}$  ( $De = 1.6$ ) (fig. 10c) we observe the onset of flow instability. The flow structures become asymmetric and there is

significant lane changing.

We now try to understand this increased flow instability and its effect on increased flow resistance using  $De$  and  $El$  numbers (defined earlier). Figure 2 shows the typical relaxation time for the viscoelastic surfactant solutions for different molar concentrations ratio of CTAB and NaSal. For a 2mM solution the relaxation time is around 0.005 s. Based on this, the critical  $De$  number ( $De_c = \tau_c \gamma_{app,mic}$ ) for pillared channel (P16) is around 0.85 (shear rate corresponding to the onset of flow thickening is obtained from figure 9). Thus after the critical  $De$  of 0.85, the wormlike micelles starts to shear thicken. At similar shear rate  $Re$  number is  $< 0.01$ . So the elasticity number  $El = \tau_c \eta / k \rho$  is more than 85. After the critical shear rate the VES starts to shear thicken, so the viscosity increases, thus  $El$  increases also. At the flow rate of 2  $\mu\text{l}/\text{min}$  the  $De$  number already crosses the critical  $De$  of 0.85. Thus the viscoelastic surfactants do not get sufficient time to relax. At such high shear rates the extensional effects are found to be predominant<sup>23</sup>. These strong extensional and shear effects might initiate the spatial and temporal fluctuations. The VES streamlines are found to follow preferential flow paths – there are slow and fast co-moving lanes – even though the  $Re$  number is extremely low. The time dependent nature of the flow profiles is observed clearly in the figure 12, which shows the flow profile (averaged over 20 frames) at successive time intervals. The images show the existence of strong temporal instability in the pillared microchannel. This further proves that no stable gel formation occurs in the range of flow rates studied here, as no permanent blockage was observed throughout the microchannel. Figure 9, shows that for the 2.0/2.0 mM solution at a flow rate of 0.5  $\mu\text{l}/\text{min}$  the VES solution is in a pseudo-Newtonian regime, however at 3  $\mu\text{l}/\text{min}$ , the VES solution is in a steeply shear thickening regime. We can correlate the instability with the SIS formed in the shear thickening regime. At flow rate  $< 1$   $\mu\text{l}/\text{min}$ , the VES shows symmetric flow behavior. At a flow rate of 2  $\mu\text{l}/\text{min}$  when the flow instability is observed, the flow resistance is around 17 times. The value of  $El$  becomes  $> 1000$ , from a value of 85 in the

pseudo Newtonian regime. However, at a larger flow rate ( $> 3 \mu\text{l}/\text{min}$ ), the shear thinning response of the fluid decreases the viscosity, effectively lowering the elasticity number. This leads to a decreased flow instability at higher shear rates. This shows that the SIS are transient in nature and break at higher shear rates also in pressure driven flow.

#### **4. CONCLUSION**

In this work we experimentally show that the flow behavior of a wormlike micellar solution through a model porous media is more complex compared to its Newtonian counterpart, even in the creeping flow regime. For the VES solution, enhanced flow resistance occurs at a similar critical shear rate in the packed bed and in the pillared microchannel of identical permeability. However, the threshold is at a much higher shear rate for Couette flow. The flow resistance factor (a measure of apparent viscosity) is highest for the core flow, followed by the microchannel and then simple shear (Couette) flow for the same VES concentration. This is a consequence of more complex fluid-structure interaction in the 3D packed bed and pillared microchannel than a simple shear flow. The microfluidic experiments reveal that the flow profiles of the VES solution show a strong spatial and temporal instability. The onset of this instability (corresponding to a critical De number) directly corresponds to the shear rate when the VES starts to shear thicken. This instability is accompanied by lane changes in the pillared channel and the presence of preferred lanes. Detailed analysis reveals that in the three-dimensional packed bed, higher deformation rates can induce larger shear and extensional effects, leading to a stronger and stable SIS formation. Thus the packed bed shows a higher flow resistance compared to the microchannel (of similar permeability) at the same shear rate. To the best of our knowledge, existence of such flow instability for viscoelastic surfactant flow through pillared microchannel, and its relation to an enhanced flow resistance has not been reported before. The experiments further prove that microchannels with specific arrangements of obstacles can be used to study the interaction between complex fluid rheology and flow

topology of viscoelastic surfactant flow through porous media.

### **ACKNOWLEDGEMENT**

We thank Prof. Hans Kuipers, Dr. Frank Peters and Dr. John van der Schaaf for technical discussions and valuable suggestions

## REFERENCES

1. Anderson VJ, Pearson JRA, Boek ES. The rheology of wormlike micellar fluids. 2006;2006:217-253.
2. Pope TL, Olsen T, Powers B, Wilson A. Expanding Applications for Viscoelastic Surfactants. :10-23.
3. Lake, L.W., Johns, R.T., Rossen, W.R. and Pope G. Fundamentals of Enhanced Oil Recovery. Society of Petroleum Engineers; 1986.
4. Dullien FAL. Porous Media-Fluid Transport and Pore Structure. Academic, New York; 1979.
5. Moss GR, Rothstein JP. Flow of wormlike micelle solutions past a confined circular cylinder. *J.Nonnewton.Fluid.Mech.*2010;165(21-22):1505-1515.
6. Chhabra RP, Comiti J, Macha. Flow of non-Newtonian fluids in fixed and fluidised beds. *Chem Eng Sci.* 2001;56(1):1-27.
7. J.N. Israelachvili. Intermolecular and Surface Forces: With Applications to Colloidal and Biological Systems,.; 1985.
8. Shikata T, Hirata H. Micelle Formation of Detergent Molecules in Aqueous Media . 2 . Role of Free Salicylate Ions on Viscoelastic Properties of Aqueous Cetyltrimethylammonium Bromide-Sodium Salicylate Solutions. 1988;(3):1081-1086.
9. H H, Rehage H, Platz G, Schorr W, Thurn H, Ulbricht W. Investigations on a detergent system with rodlike micelles. 1982;1056:1042-1056.
10. Nettesheim F, Wagner NJ. Fast Dynamics of Wormlike Micellar Solutions. 2007;(8):5267-5269.
11. Menon SVG, Goyal PS, Dasannacharya BA, Paranjpe SK, Mehta R V., Upadhyay R V. When does a living polymer live? - Case of CTAB/NaSal. *Phys B Phys Condens Matter.* 1995;213-214(C):604-606.
12. Moss GR, Rothstein JP. Flow of wormlike micelle solutions past a confined circular cylinder. *J.Nonnewton.Fluid.Mech.*2010;165(21-22):1505-1515.
13. Rothstein JP. Strong Flows of Viscoelastic Wormlike Micelle Solutions. *Rheol Rev.* 2008;2008:1-46.
14. Cates ME. Reptation of Living Polymers: Dynamics. 1987;2289-2296.
15. Boek ES, Padding JT, Anderson VJ, Briels WJ, Crawshaw JP. Flow of entangled wormlike micellar fluids : Mesoscopic simulations , rheology and PIV experiments. *J.Nonnewton.Fluid.Mech.* 2007;146:11-21.
16. Olmsted P. Statics and dynamics of worm-like surfactant micelles.
17. Torres MF, Sa AE. Effect of the Flow Field on the Rheological Behavior of Aqueous Cetyltrimethylammonium p -Toluenesulfonate Solutions. 2004;(26):3838-3841.
18. Hartmann V, Cressely R. Simple salts effects on the characteristics of the shear thickening exhibited by an aqueous micellar solution of CTAB/NaSal. *Europhys Lett.* 2007;40(6):691-696.
19. Kadoma IA, Egmond JW Van. Structural transitions in wormlike micelles. 1997;12:1-12.
20. Kadoma IA, Egmond JW Van. Shear-Enhanced Orientation and Concentration Fluctuations in Wormlike Micelles : Effect of Salt. 1997;7463(9):4551-4561.

21. Dogon D, Golombok M. Self-regulating solutions for proppant transport. *Chem Eng Sci.* 2016;148:219-228.
22. Hu Y, Wang SQ, Jamieson AM. Rheological and flow birefringence studies of a shear-thickening complex fluid — A surfactant model system Rheological and flow birefringence studies of a shear- thickening complex fluid-A surfactant model system. 2000;531(1993).
23. Hu Y, Wang SQ, Jamieson a. M. Elongational Flow Behavior of Cetyltrimethylammonium Bromide/Sodium Salicylate Surfactant Solutions. *J Phys Chem.* 1994;98(34):8555-8559..
24. Pakdel P, McKinley G. Elastic Instability and Curved Streamlines. *Phys Rev Lett.* 1996;77(12):2459-2462.
25. Groisman A, Steinberg V. Elastic turbulence in a polymer solution flow. *Nature.* 2000;405(6782):53-55.
26. Bodiguel H, Beaumont J, Machado A, Martinie L, Kellay H, Colin A. Flow enhancement due to elastic turbulence in channel flows of shear thinning fluids. *Phys Rev Lett.* 2015;114(2):1-5.
27. Pan L, Morozov A, Wagner C, Arratia PE. Nonlinear elastic instability in channel flows at low reynolds numbers. *Phys Rev Lett.* 2013;110(17):1-5..
28. Shaqfeh ES. Fully Elastic Instabilities in Viscometric Flows. *Annu Rev Fluid Mech.* 1996;28(1):129-185.
29. Larson RG, Shaqfeh ES., Muller SJ. A purely elastic instability in Taylor Couette flow. *J Fluid Mech.* 1990;218:573-600.
30. De, S., van der Schaaf, J., Deen, N. G., Kuipers, J. A. M., Peters, E. A. J. F., & Padding JT. Elastic Instabilities in Flows through Pillared Micro channels. *arXiv Prepr arXiv.* 2016;1607.03672.
31. De S, Das S, Kuipers JAM, Peters EAJF, Padding JT. A coupled finite volume immersed boundary method for simulating 3D viscoelastic flows in complex geometries. *J Nonnewton Fluid Mech.* 2016;232:67-76.
32. Hulsén MA, Fattal R, Kupferman R. Flow of viscoelastic fluids past a cylinder at high Weissenberg number: Stabilized simulations using matrix logarithms. *J Nonnewton Fluid Mech.* 2005;127(1):27-39.
33. Smith MD, Joo YL, Armstrong RC, Brown RA. Linear stability analysis of flow of an Oldroyd-B fluid through a linear array of cylinders. *J Nonnewton Fluid Mech.* 2002;109(1):13-50.
34. Liu AW, Bornside DE, Armstrong RC, Brown RA. Viscoelastic flow of polymer solutions around a periodic, linear array of cylinders: comparisons of predictions for microstructure and flow fields. *J Nonnewton Fluid Mech.* 1998;77(3):153-190.
35. Souvaliotis A, Beris AN. Spectral collocation/domain decomposition method for viscoelastic flow simulations in model porous geometries. *Comput Methods Appl Mech Eng.* 1996;129(1-2):9-28.
36. Vázquez-Quesada A, Ellero M. SPH simulations of a viscoelastic flow around a periodic array of cylinders confined in a channel. *J Nonnewton Fluid Mech.* 2012;167-168:1-8.
37. Gillissen JJJ. Viscoelastic flow simulations through an array of cylinders. *Phys Rev E - Stat Nonlinear, Soft Matter Phys.* 2013;87(2):1-7. doi:10.1103/PhysRevE.87.023003.
38. Hua CC, Schieber JD. Viscoelastic flow through fibrous media using the CONNFFESSIT approach. *J Rheol.* 1998;42(3):477.
39. Rothstein JP, McKinley GH. The Axisymmetric Contraction-Expansion: The Role of Extensional Rheology on Vortex Growth Dynamics and the Enhanced Pressure Drop. *J Nonnewton Fluid Mech.* 2001:98
40. Louis S. Anomalous pressure drop behaviour of mixed kinematics flows of viscoelastic

- polymer solutions: a multiscale simulation approach. 2009;631:231-253.
41. De S, Kuipers JAM, Peters EAJF, Padding JT. Viscoelastic flow simulations in model porous media. *Phys Rev Fluids*. 2017;2(5):53303.
  42. Rojas MR, Müller AJ, Sáez AE. Shear rheology and porous media flow of wormlike micelle solutions formed by mixtures of surfactants of opposite charge. *J Colloid Interface Sci*. 2008;326(1):221-226.
  43. Vasudevan M, Buse E, Lu D, et al. Irreversible nanogel formation in surfactant solutions by microporous flow. *Nat Mater*. 2010;9(5):436-441.
  44. Zhao Y, Shen Q, Haward SJ. Soft Matter Flow of wormlike micellar solutions around confined microfluidic cylinders †. *Soft Matter*. 2016.
  45. Nilsson MA, Kulkarni R, Gerberich L, et al. Effect of fluid rheology on enhanced oil recovery in a microfluidic sandstone device. *J Nonnewton Fluid Mech*. 2013;202:112-119.
  46. Cardiel JJ, Dohnalkova AC, Dubash N, Zhao Y, Cheung P, Shen AQ. Microstructure and rheology of a flow-induced structured phase in wormlike micellar solutions. *Proc Natl Acad Sci U S A*. 2013;110(18):E1653-60.
  47. Victor Lifton. 2016 Microfluidics an enabling screening technology for enhanced oil recovery (EOR). *Lab Chip*. 2016:1-43.
  48. De Loos SRA, Van Der Schaaf J, Tiggelaar RM, Nijhuis TA, De Croon MHJM, Schouten JC. Gas-liquid dynamics at low Reynolds numbers in pillared rectangular micro channels. *Microfluid Nanofluidics*. 2010;9(1):131-144.
  49. Sousa PC, Pinho FT, Oliveira MSN, Alves MA. Efficient microfluidic rectifiers for viscoelastic fluid flow. *J Nonnewton Fluid Mech*. 2010;165(11-12):652-671.

**List of tables:**

Table 1. Shear properties of the VES solutions

CTAB/NaSal (mM/mM)	$\gamma_c$ ( $s^{-1}$ )	$\mu_0$ (mPa · s)	$\mu_{max}$ (mPa · s)
1.0/1.0	365	1.2	1.9
1.5/1.5	296	1.3	2.4
2.0/2.0	193	1.5	3.7

Table 2. Dimensions of different microchannels used in this study

Channel	Pillar diameter ( $\mu\text{m}$ ) ( $D_p$ )	X – pitch ( $\mu\text{m}$ ) ( $X_p$ )	Y- pitch ( $\mu\text{m}$ ) ( $Y_p$ )	Porosity ( $\epsilon$ )	Permeability (mD) ( $K$ )
1 (P5)	4	4.6	10.8	0.80	4000
2 (P16)	16	32.0	60.0	0.89	8500

**List of Figure captions:**

Figure 1. Simple shear rheology of different VES solutions compared to brine at 22 °C ( $\mu_0, \mu_{max}$  and  $\gamma_c$  corresponds to zero shear viscosity, maximum shear viscosity and critical shear rate respectively)

Figure 2. Relaxation time of VES solution for different CTAB/NaSal molar concentration ratio

Figure 3. Core flow experiment with sintered glass core (Arrow shows the flow direction)

Figure 4 (a). Geometry of a typical pillared microchannel (n, m shows the number of pillars in the x (flow) and y direction) (b) SEM image of the microchannel showing the alignment of the pillars

Figure 5. Flow rate plotted against pressure gradient for three different VES fluids flow through a 4400 mD sintered glass core at 22 °C. Dashed line represents the Newtonian case

Figure 6. Resistance factor plotted against flow rate for three different equimolar solutions through a 4400 mD sintered glass core at 22 °C

Figure 7. Flow rate vs. pressure gradient for brine and 2.0/2.0 VES solution in P16  $\mu$ -channel

Figure 8. Resistance factor at different flow rates for a 2.0/2.0 mM VES solution in two different micro-channel; P5 & P16

Figure 9. Resistance factor at different flow rates for three different VES fluids in the P16 micro channel

Figure 10. Resistance factor against apparent shear rate for 2.0/2.0 VES solution in rheometer, sintered glass core and P5 micro-channel

Figure 11. Trajectories of tracer particles in P16 microchannel for (a) brine at 3  $\mu\text{l}/\text{min}$ , (b) VES 2.0/2.0 at 0.5  $\mu\text{l}/\text{min}$ , and (c) VES 2.0/2.0 at 3  $\mu\text{l}/\text{min}$  (flow direction is from right to left, the color bar shows the occupancy)

Figure 12. (a)- (d) Time averaged trajectories of tracer particles in P16 microchannel for VES 2.0/2.0 at 3  $\mu\text{l}/\text{min}$  at different times (flow direction is from right to left, the color bar shows the occupancy)

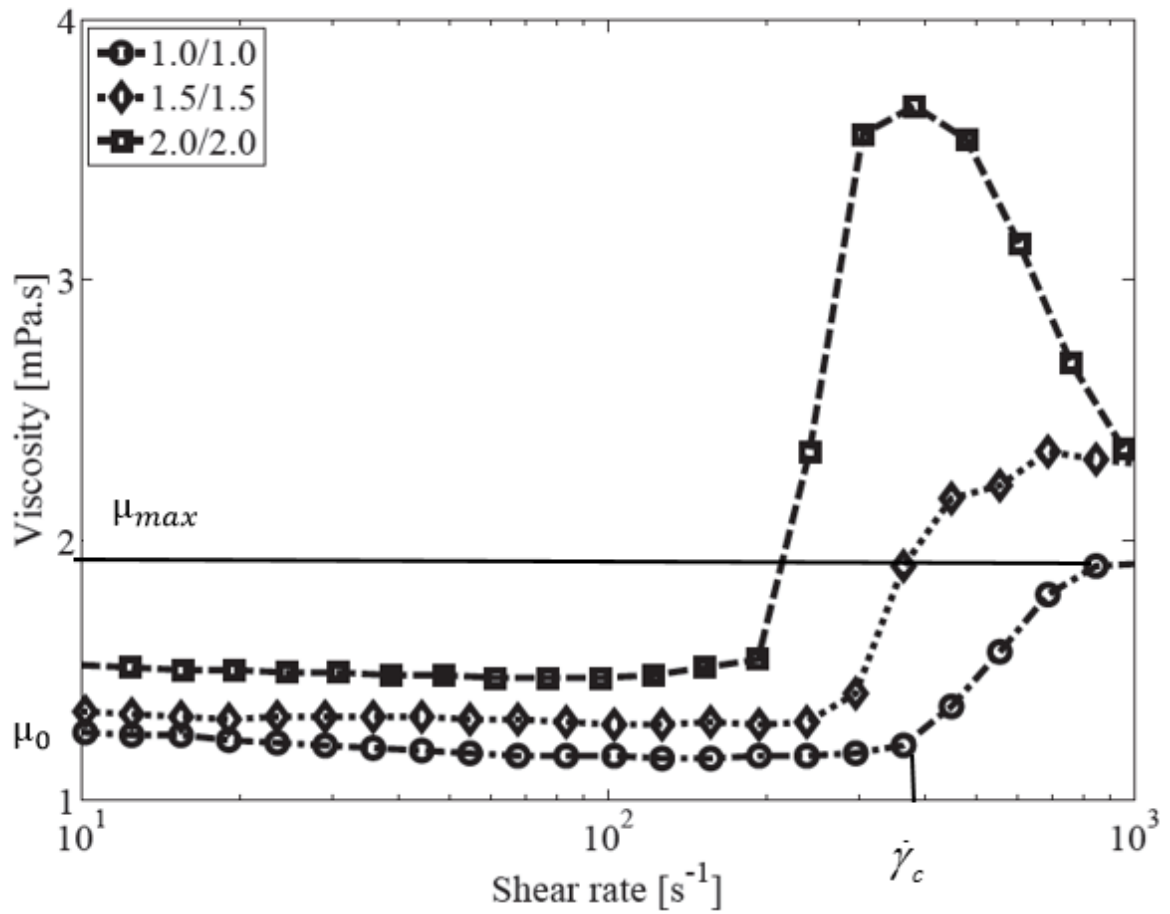


Figure 1. Bulk shear rheology of different VES solutions compared to brine at 22 °C ( $\mu_0, \mu_{max}$  and  $\gamma_c$  correspond to zero shear viscosity, maximum shear viscosity and critical shear rate, respectively, for the case of the 1.0/1.0 mM solution)

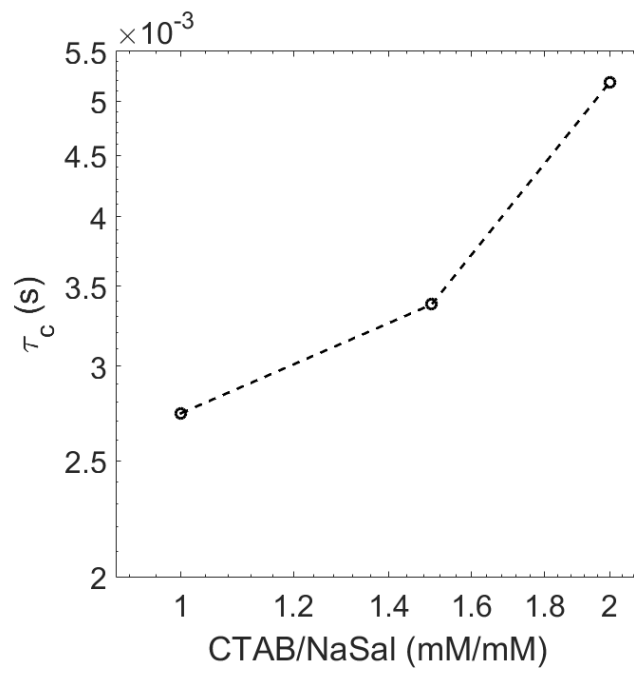


Figure 2. Relaxation time of the VES solution for different CTAB/NaSal molar concentrations

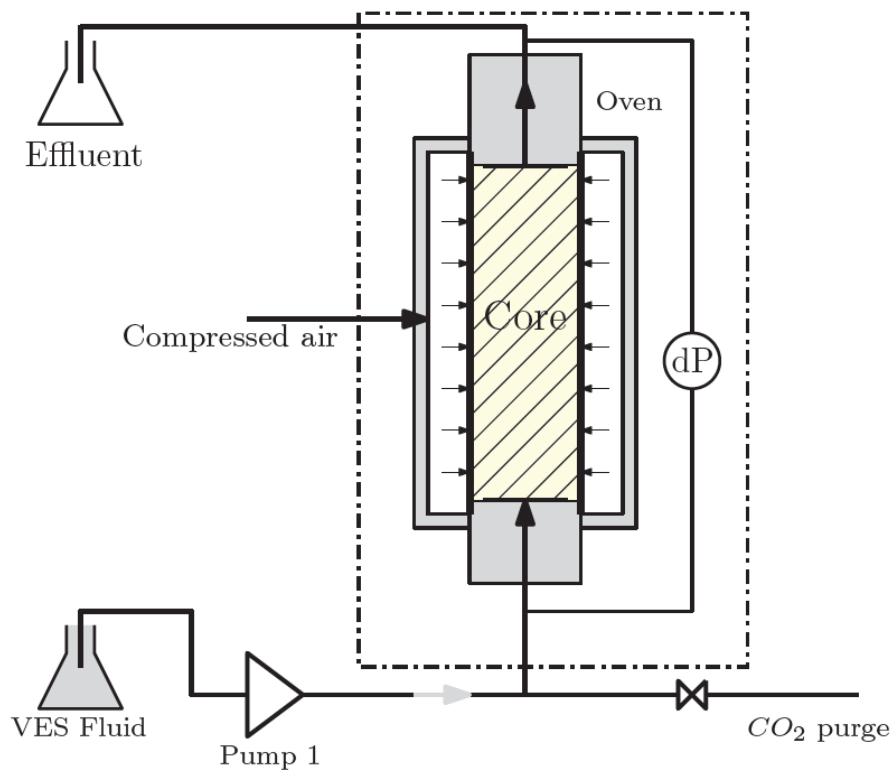


Figure 3. Core flow experiment with sintered glass core (arrows show the flow direction)

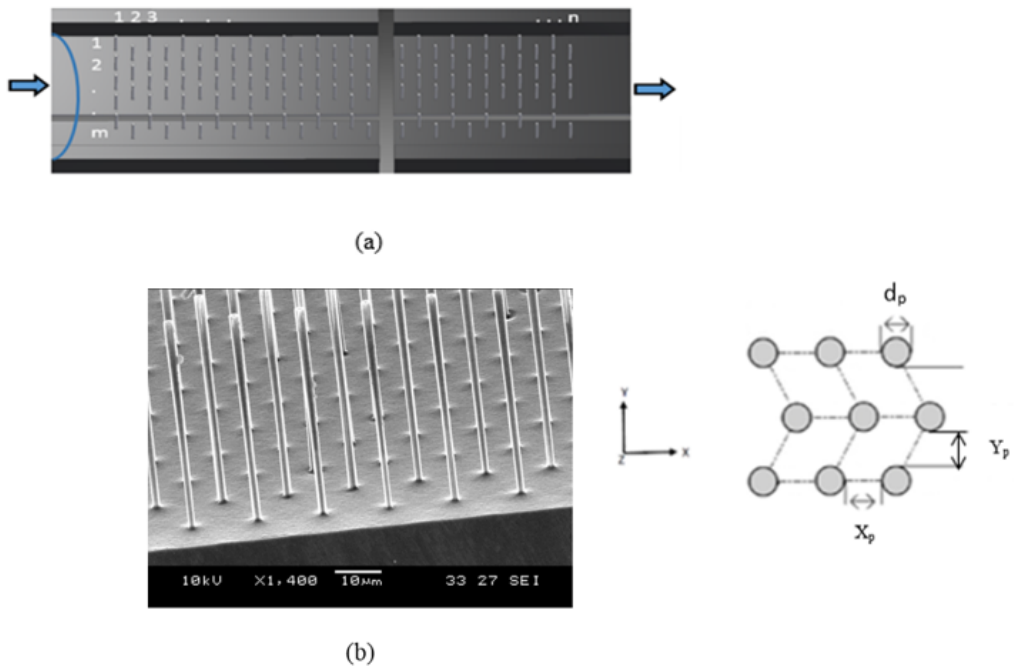


Figure 4 (a). Geometry of a typical pillared microchannel ( $n$ ,  $m$  shows the number of pillars in the  $x$  (flow) and  $y$  direction) (b) SEM image of the microchannel showing the alignment of the pillars

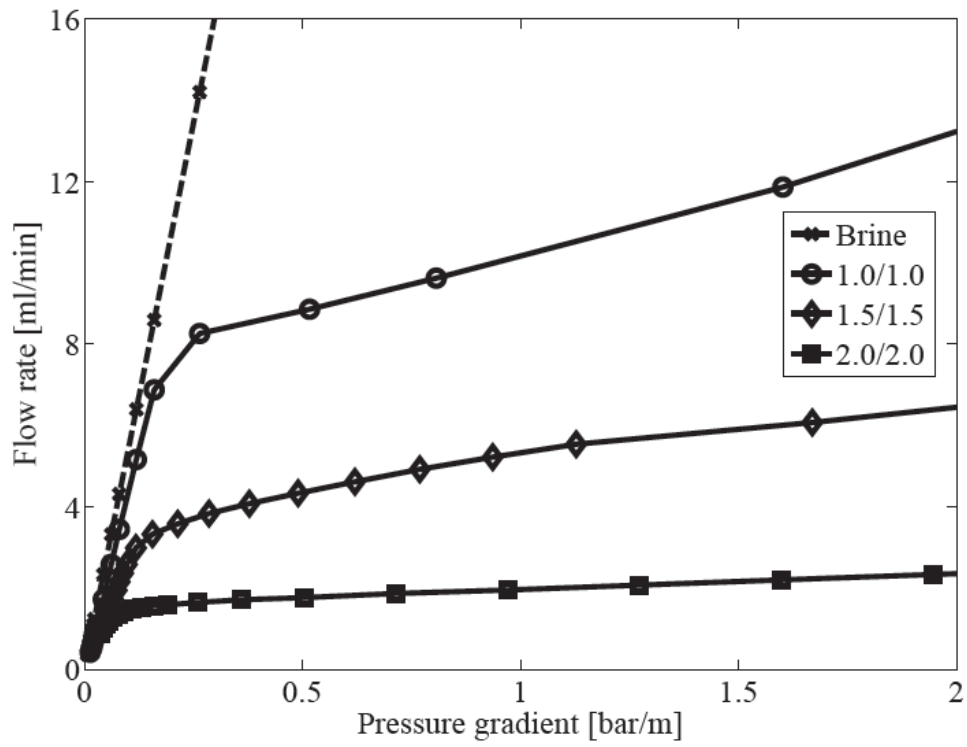


Figure 5. Flow rate plotted against pressure gradient for three different VES fluids flowing through a 4400 mD sintered glass core at 22 °C. Dashed line represents the Newtonian case

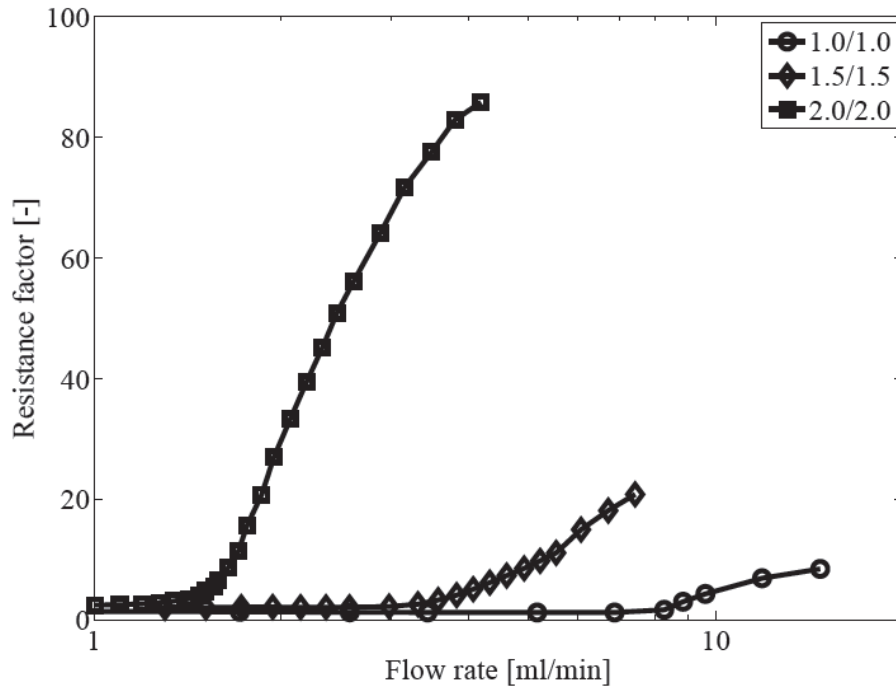


Figure 6. Resistance factor plotted against flow rate for three different equimolar solutions through a 4400 mD sintered glass core at 22 °C

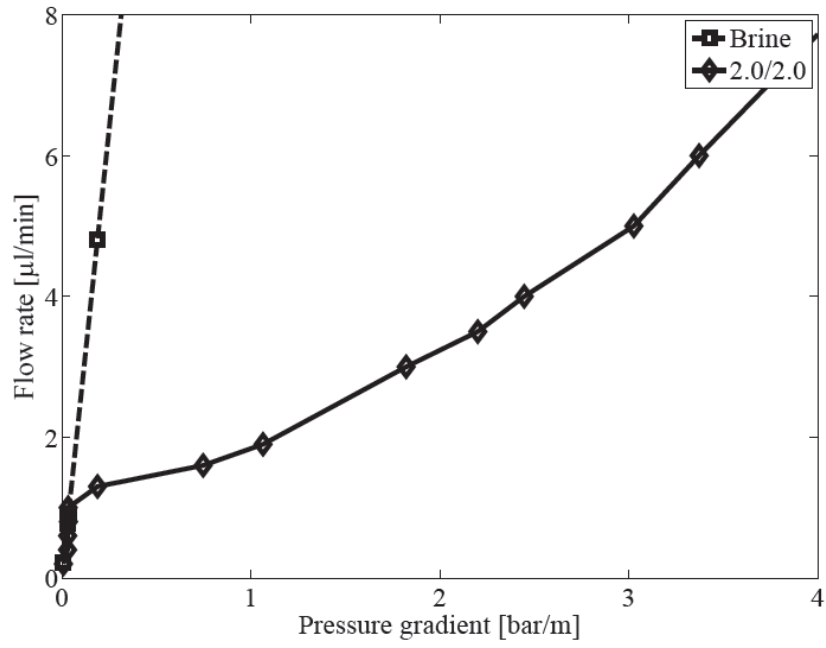


Figure 7. Flow rate vs pressure gradient for brine and 2.0/2.0 VES solution in the P16 micro-channel

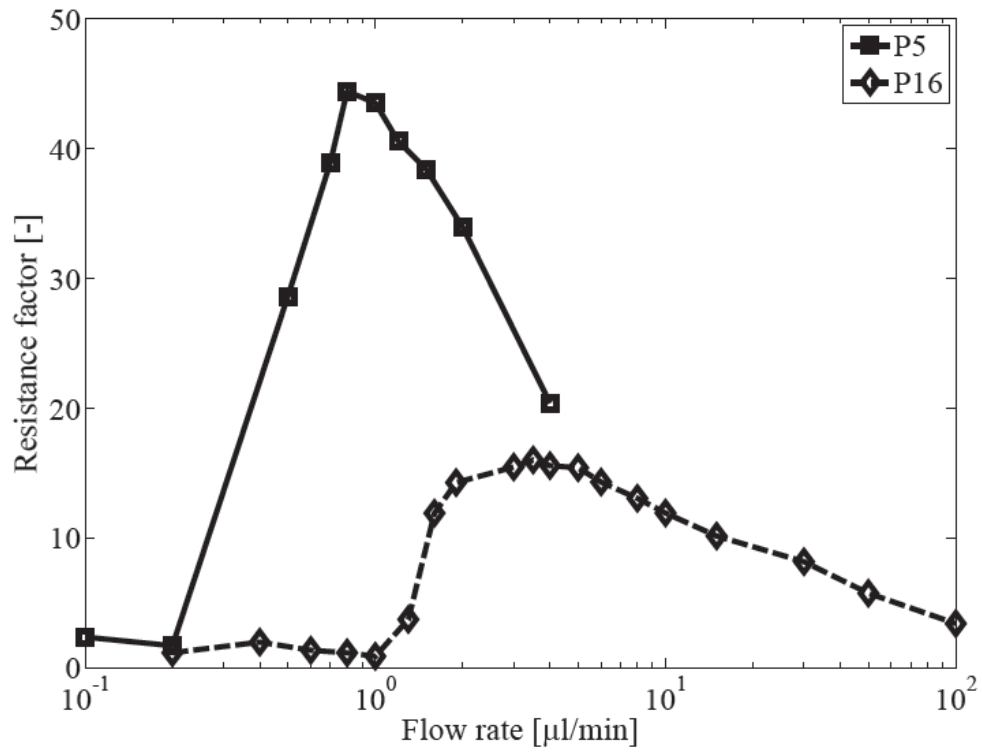


Figure 8. Resistance factor at different flow rates for a 2.0/2.0 mM VES solution in two different micro-channels: P5 & P16

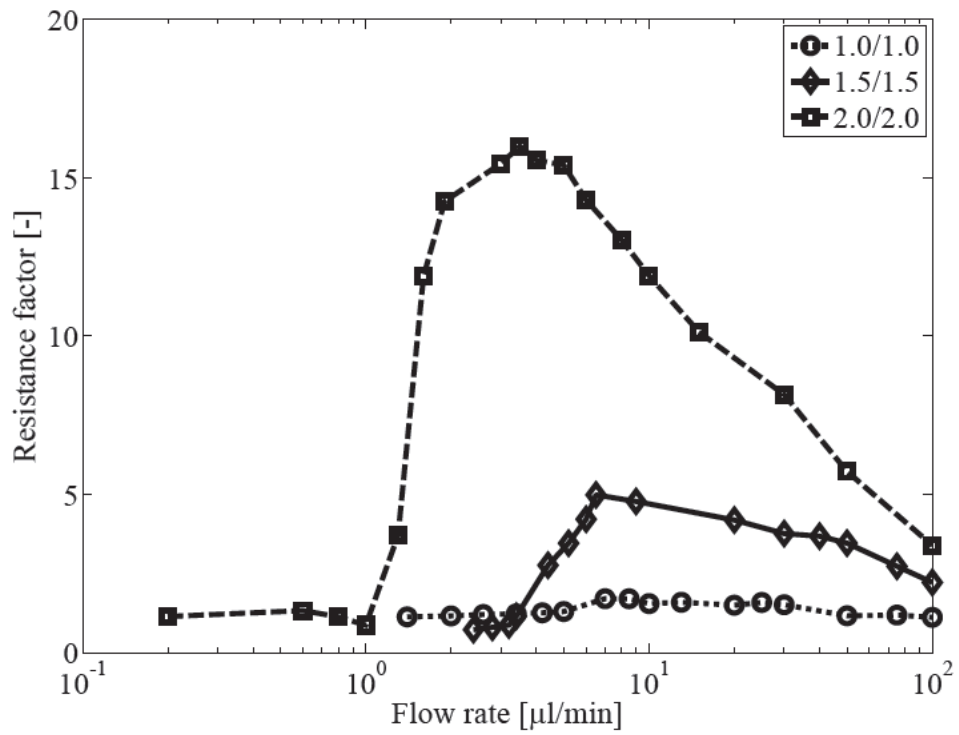


Figure 9. Resistance factor at different flow rates for three different VES fluids in the P16 micro channel

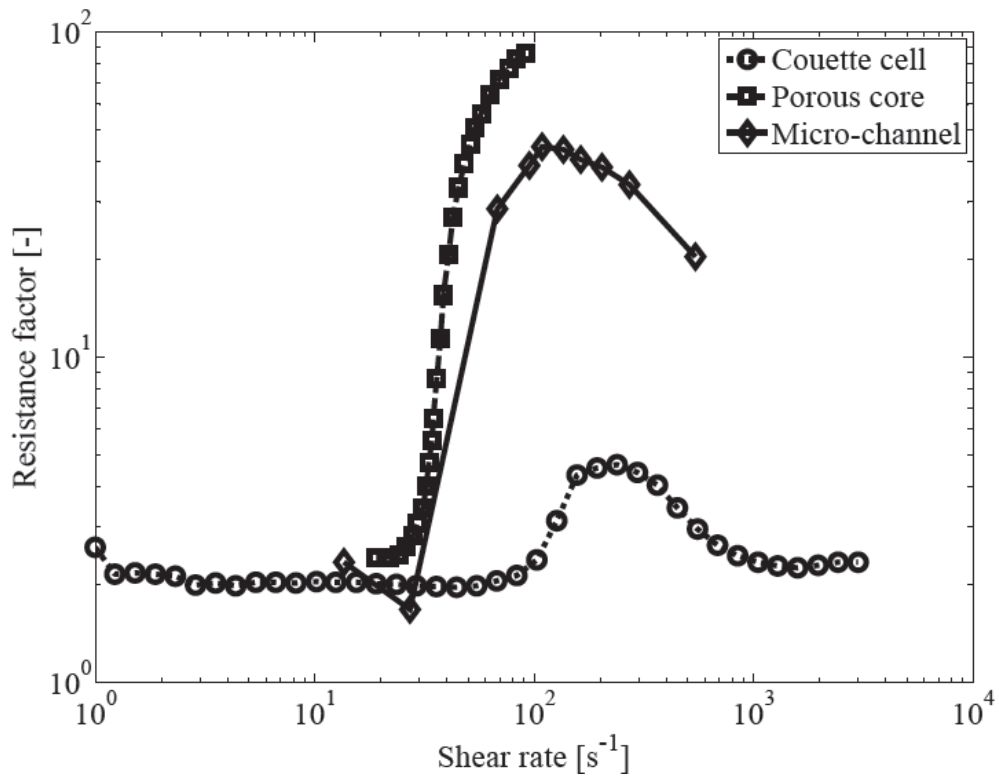


Figure 10. Resistance factor against apparent shear rate for 2.0/2.0 VES solution in rheometer, sintered glass core and P5 micro-channel

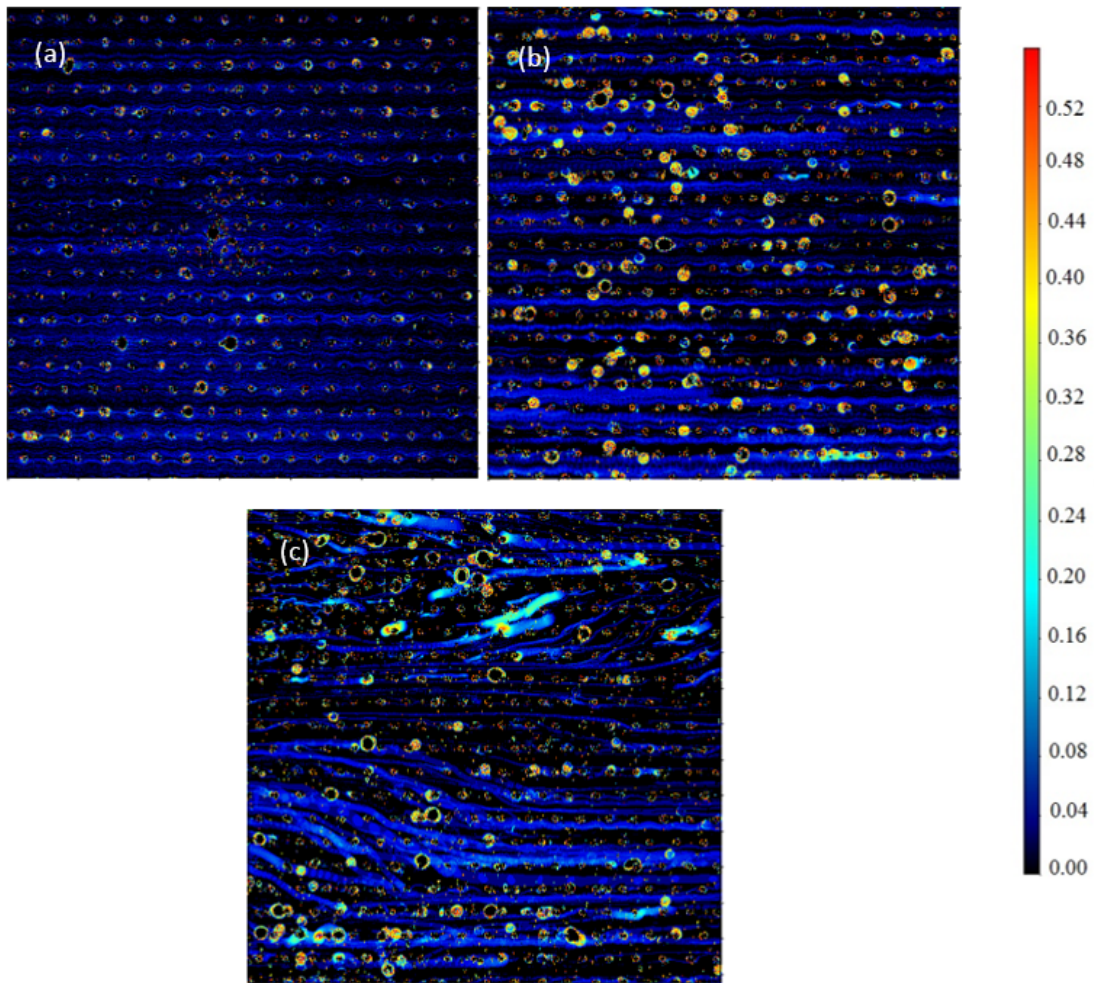


Figure 11. Trajectories of tracer particles in P16 microchannel for (a) brine at 3  $\mu\text{l}/\text{min}$ , (b) VES 2.0/2.0 at 0.5  $\mu\text{l}/\text{min}$ , and (c) VES 2.0/2.0 at 3  $\mu\text{l}/\text{min}$  (flow direction is from right to left, the color bar shows the occupancy)

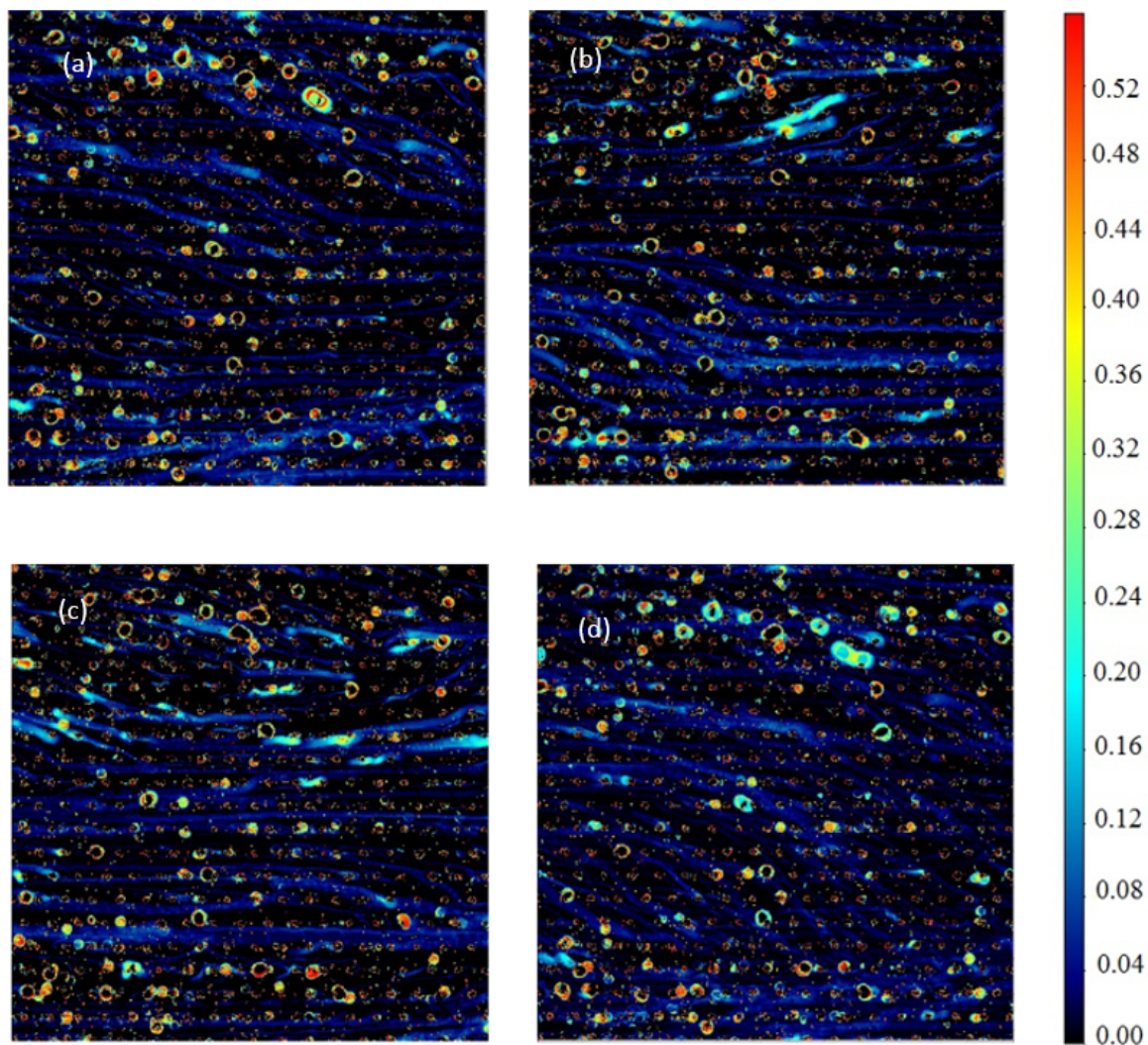


Figure 12. (a)- (d) Time averaged trajectories of tracer particles in P16 microchannel for VES 2.0/2.0 at 3  $\mu\text{l}/\text{min}$  at different times (flow direction is from right to left, the color bar shows the occupancy)